Inline Edge Illumination Computed Tomography: A Simulation Study

Verstraete Jitse
imec-Vision Lab
University of Antwerp
Antwerp, Belgium
jitse.verstraete@uantwerpen.be

Francken Nicholas
imec-Vision Lab
University of Antwerp
Antwerp, Belgium
nicholas.francken@uantwerpen.be

Sijbers Jan
imec-Vision Lab
University of Antwerp
Antwerp, Belgium
jan.sijbers@uantwerpen.be

De Beenhouwer Jan
imec-Vision Lab
University of Antwerp
Antwerp, Belgium
jan.debeenhouwer@uantwerpen.be

***Abstract*—Due to the growing demand for inspection in the context of Industry 4.0, non-destructive testing is predominantly performed inline by irradiating a sample and measuring the intensity loss caused by X-ray attenuation. This results in a 2D attenuation-based projection image. Combining multiple projection images taken at different angular views, allows the creation of a 3D reconstruction of the sample. With dedicated setups, additional contrasts can also be recovered, such as phase contrast. Combining phase-sensitive X-ray techniques with full 3D reconstructions has the potential to significantly enhance the information gained during inspection. A 2D inline acquisition method has previously been demonstrated using a modified edge illumination phase contrast setup, allowing the retrieval of both attenuation and phase contrast by measuring an illumination curve. Extending this approach to 3D, however, remains a challenge, requiring a novel acquisition scheme that integrates sample translation, rotation and illumination curve sampling. In this paper, we propose a flexible inline edge illumination CT method that facilitates this extension without hardware modifications, while offering freedom in parameters, such as the number of projection angles and illumination curve points. Through a realistic simulation study, we show that the proposed method can be applied for inline inspection without increasing the number of required projections compared to conventional edge illumination X-ray imaging.**

***Index Terms*—Industry 4.0, inline inspection, non-destructive testing, X-ray phase contrast computed tomography, edge illumination.**

I. Introduction

X-ray imaging is widely used in non-destructive testing to detect defects or other anomalies in objects. Using the attenuation properties of X-rays when passing a sample, projection images can be constructed that provide structural and internal information of the sample. However, all depth information is lost. In X-ray computed tomography (XCT), this information is retained by taking multiple projections at different angular views and creating a 3D model of the inspected sample. A surface mesh of this model is extracted and compared to a ground truth, available in the form of a computer-aided design (CAD) model. The use of XCT for industrial inspection has already been validated in fields such as additive manufacturing [1], food quality control [2] and polymer weld inspection [3].

X-ray attenuation-based XCT has limitations in detecting defects in materials with similar densities. This is, for example, problematic when inspecting lightweight polymer-based composite materials, which are increasingly used in critical applications due to their superior strength-to-weight ratios [4]. X-ray phase contrast imaging (XPCI) uses the refraction of X-rays to provide an improved contrast for these low-attenuating materials. Refraction occurs when X-rays transition from one medium to another with different refractive indexes, for example at cracks and at the interfaces between boundaries. This makes XPCI a more ideal imaging modality in numerous industrial applications, such as quality control [5] and material sciences [6].

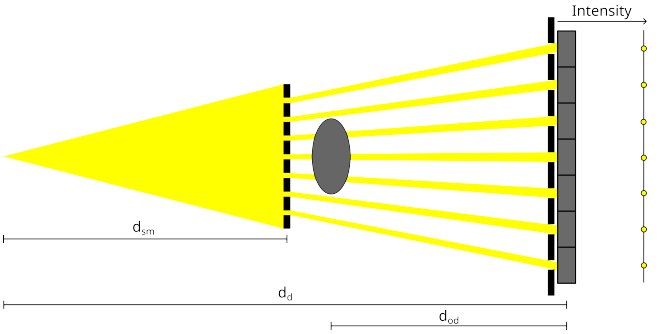

Fig. 1: The conventional EI setup (not to scale). Two masks can be seen: the sample mask, placed between the X-ray source and sample, and the detector mask, placed in front of the detector. The measured intensity across the detector is shown on the right.

This work was funded by the Research Foundation Flanders (FWO) project FoodPhase (S003421N) and UA IOF-POC project X4Food (FFI240371).

Edge Illumination (EI) is an XPCI technique that allows the visualization of both attenuation and phase contrast [7]. The EI setup is illustrated in Fig. 1. Two absorbing masks with periodic slits are used: the sample mask and the detector mask. The sample mask splits the X-ray beam in multiple beamlets that can be perfectly aligned with the apertures of the detector mask. However, depending on the lateral shift of the sample mask, these beamlets can also be be partially absorbed, or fully blocked by the detector mask. By taking multiple projections at different lateral positions, an approximately Gaussian pixel-wise intensity curve (IC) can be measured for every pixel and angle. The relative change of these ICs when an object is positioned between both masks, allows the retrieval of attenuation and phase contrast.

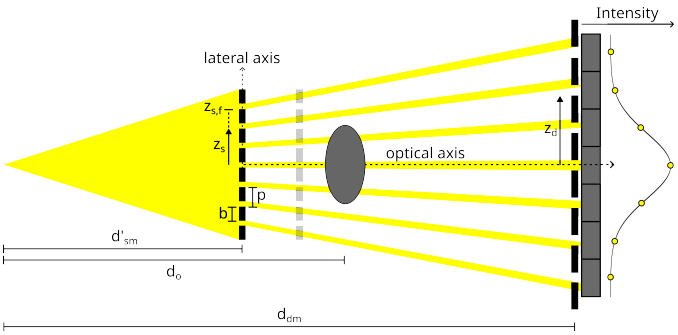

Fig. 2: The out-of-focus EI setup (not to scale). The original mask position is shown in light grey. The optical axis shift increases the projected period of the sample mask apertures, causing a mismatch at the detector mask. The resulting intensity modulation can be seen at the right.

Conventional EI requires movement of the sample mask in order to sample the IC curve. Data acquisition in the industry is, however, predominantly performed inline using static setups, making conventional EI unsuitable for inline acquisition. Three 2D acquisition approaches have already been proposed that avoid sample mask movement: single-shot acquisition [8], asymmetric masks [9] and out-of-focus EI [10]. Single-shot acquisition requires the assumption of quasi-homogeneous samples, which is not always applicable for industrial samples. The asymmetrical masks and out-of-focus technique break the perfect alignment between the sample mask and detector mask, which changes the detector mask absorption of the beamlets and in turn their measured intensity. This corresponds to the measurement of different IC points. In the asymmetric mask setup, the apertures of the sample mask are shifted to create a mismatch with the detector mask. This is however not compatible with conventional EI and changing the mask mismatch requires the fabrication of a new mask. The out-of-focus technique (see Fig. 2) introduces a mismatch by shifting the sample mask along the optical axis. This changes the period of the sample mask apertures projected onto the detector mask, resulting in a different detector mask absorption for every beamlet. An intensity modulation is produced across the detector which can be linked to different IC points. This means that sampling the IC does not require translation of the sample mask, but translation of the sample itself, which integrates well with the conveyor belt movement often used in inline acquisition. Depending on the size of the optical shift, the shape of this modulation curve can be tuned. In Fig. 2, the chosen optical axis shift creates a full IC across the detector. Choosing an even bigger shift, increases the projected period of the sample mask apertures until some beamlets start to enter adjacent detector mask apertures. This results in the creation of additional ICs across the detector (see Fig. 5). The corresponding IC points have already been measured. This makes the number of unique IC points tunable.

Even though the use of an XPCI technique for industrial radiography-based inspection has been experimentally validated in the past, the extension to full 3D reconstructions has never been made [10]. In this paper, an acquisition scheme will be created that transforms the out-of-focus EI technique into a phase-sensitive EI XCT technique, providing full reconstructions for both attenuation and phase contrast. The acquisition scheme will provide a high degree of freedom in number of IC points and projection angles. First, the inline out-of-focus XCT method will be explained, after which its performance will be validated using the software CAD-ASTRA, a mesh-based simulation toolbox for X-ray projection data [11]. The method will be tested in the context of inline fruit inspection.

II. Methods

A. Inline out-of-focus EI radiography

Determining transmission and refraction is based on the measurement of ICs. For conventional EI, the sample mask and detector mask are aligned perfectly [7], so that the beamlets fit in the apertures of both masks. The ICs itself can be retrieved by measuring the intensity in every pixel for different sample mask steps. Due to detector blurring and a finite source spot size, the ICs can be approximated by Gaussian curves. The relative change of its parameters before and after introducing a sample, can be linked to the two contrasts:

$$\begin{aligned} T &= \frac{A_s \sigma_s}{A_f \sigma_f} \\ \alpha &= \frac{M}{d_{od}} \left(\mu_s - \mu_f\right) \end{aligned} \tag{1}$$

with T and α the pixel-wise transmission and refraction angle signal respectively, $M = d_d/d_o$ the geometric magnification and $A_{f,s}$, $\mu_{f,s}$ and $\sigma_{f,s}$ the amplitude, peak position and standard deviation of the flatfield and sample ICs respectively. d_d is the source-detector distance, d_o the source-object distance and d_{od} the object-detector distance. Attenuation contrast can be retrieved by applying the Beer-Lambert law on the transmission signal. Retrieving phase contrast requires an integration of the refraction signal [12].

To transform the conventional EI setup into an out-of-focus EI setup, two changes are made: the sample mask is shifted along the optical axis and the sample mask translations are replaced by sample translations. The optical axis shift should be chosen so that at least one IC is spread out over the full

length of the detector (see Fig. 2). Based on the adapted setup geometry, we found:

$$d'_{sm} = \frac{z_{s,f}}{z_{s,f} + a} d_{sm} \tag{2}$$

with $z_{s,f}$ the distance from the central aperture to the final sample mask aperture, $a = p - b$ the sample mask aperture width, d_{sm} the conventional source-sample mask distance and d'_{sm} the new source-sample mask distance. The bar width of the sample mask is denoted by b and the period of the sample mask by p. This equation can be generalized by incorporating the desired number of ICs across the detector $2N - 1$ (N is the number of minima at each side of the detector):

$$d'_{sm} = \frac{z_{s,f}}{z_{s,f} + Np - b} d_{sm} \tag{3}$$

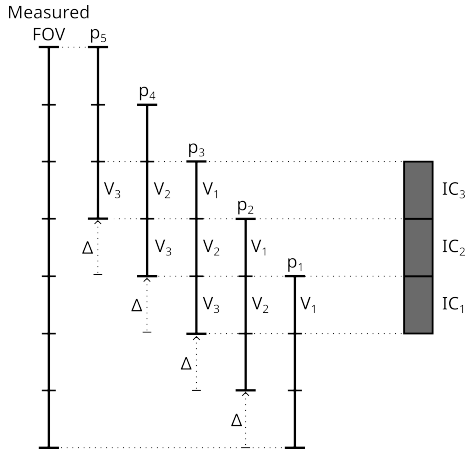

Fig. 3: Visualization of the acquisition process for out-of-focus EI radiography. The detector is shown at the right. The FOV is illustrated using lines with end markers and is divided in volumes ($V_{1,2,3}$). In total, 5 projections are needed ($2 \cdot N_{columns} - 1$). The translation step Δ and total measured FOV are also shown.

Every detector column measures a different IC point. For every projection, we can divide our sample in multiple volumes (see Fig. 3). Every volume corresponds to a beamlet and a detector column, meaning that for every volume, a unique IC point is measured. By translating our sample from one beamlet to the next, these volumes pass different detector columns, i.e. different IC sample points, which samples the ICs. This also means that the measured data needs to be reshuffled: for the first volume V_1, an IC point IC_1 is measured in the first detector column during the first projection p_1, the second IC point IC_2 of volume V_1 is measured in the second detector column during the second projection p_2, and so on. The size of the translation step is determined by the sample mask period and position:

$$\Delta = \frac{d_o}{d_{sm}} p \tag{4}$$

In conventional EI, the position of the IC points is given by the corresponding sample mask step. Due to the static setup of out-of-focus EI, this is not applicable and an equivalent mask step needs to be calculated. This can be done using the optical axis shift of the sample mask:

$$d = \frac{d_{dm}}{d'_{sm}} z_s - z_d \tag{5}$$

with z_s and z_d the sample mask and detector mask aperture distance respectively and d_{dm} the source-detector mask position.

B. Extension to inline EI XCT

In order to extend the out-of-focus technique to allow full 3D tomography, the sample must be rotated. For an inline acquisition setup, this requires the combination of rotations and translations, which can be done in multiple ways. The sample could be fully rotated during every translation step. This would collect the maximum amount of data, as every measured IC is fully sampled. However, this drastically increases the number of projections in comparison to out-of-focus radiography, nor is it ideal for continuous acquisition due to the non-constant translation speed of the sample.

Alternatively, the translation and rotation steps can be combined into one movement. For every translation step, only one projection is taken. Afterwards the sample is translated and rotated simultaneously (based on a similar approach in [13]). This acquisition method does not increase the number of projections in comparison to out-of-focus radiography, but every IC is downsampled. This can be clearly seen when dividing the sample again into multiple volumes, each corresponding to its own set of ICs (see Fig. 4). For the first projection, a maximum of one IC point is measured for every volume, similar to out-of-focus radiography. However, for radiography, the next translation step measures new IC points for the same volumes. When the sample is rotated, this is not applicable anymore. Indeed, due to rotation, the beamlets propagate through the sample at new angles. This means that the sample needs to be divided into new volumes in order to correctly match them to the different beamlets. These volumes also correspond to new sets of ICs. The next translation step thus measures IC points for these new volumes. This is repeated for the next steps until all angles have been encountered. After a full rotation, the first volumes are reencountered and new IC points can be measured. Thus, the volumes skip multiple detector columns before getting scanned again, resulting in a downsampled IC. Reshuffling of the measured sinogram is also more complex. Imagine a scan with N angles: the first IC point IC_1 of the first volume V_1 is measured in the first detector column. The next time we encounter this volume is after a full rotation, or N projection angles, resulting in N skipped detector columns. This means that the second IC point IC_{N+1} of the first volume V_1 is now measured in the detector column $N + 1$ during projection p_{N+1}. This results in a trade-off:

$$N_{columns} = N_{angles} \cdot N_{IC} \tag{6}$$

where $N_{columns}$ is the number of detector columns, N_{angles} is the number of projection angles and N_{IC} is the number of IC points. Equation 6 tells us that increasing the number of IC points requires more detector columns or a lower angular coverage.

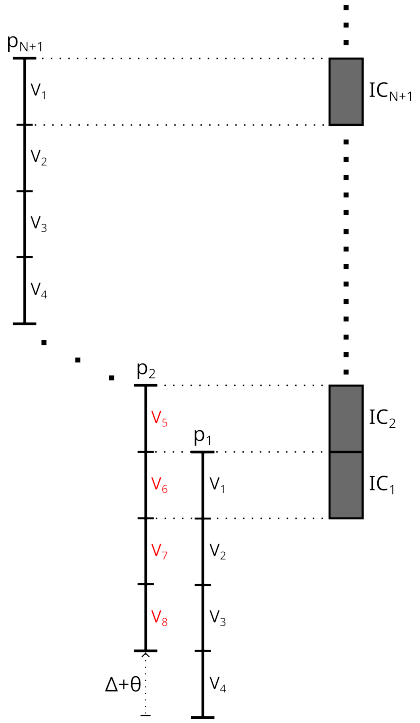

Fig. 4: Visualization of the acquisition process for out-of-focus EI XCT. The detector is shown at the right. The FOV is illustrated using lines with end markers and is divided in volumes ($V_{1,2,3,4}$). When the sample is translated (Δ) and rotated (θ), a new division in volumes needs to be made ($V_{5,6,7,8}$).

C. Acquisition process

Data acquisition with an out-of-focus EI XCT setup proceeds as follows: first, the FOV is determined. The edges of the FOV are defined by the outer two most beamlets. Analogous to section II-B, this FOV is divided into multiple volumes, each corresponding to a set of ICs. To measure all IC points for every volume in this FOV, the first projection needs to capture the first volume in the first detector column. Next, the sample is translated (along with the FOV) until the last projection captures the last volume in the last detector column (see Fig. 3). To scan one sample, a total of $2 \cdot N_{columns} - 2$ translation steps or $2 \cdot N_{columns} - 1$ projections are required. This means that the final measured FOV is almost three times as large than the original FOV. For example, the first scan only measures one volume of our FOV. All the other detector pixels still measure data however. This can later be cut off. For inline acquisition setups, two successive samples can be positioned so that their FOVs align. This way, the mean number of projections per sample can be reduced back to the number of detector columns. This avoids the measurement of unused data and increases throughput.

III. Experiments

All simulations were performed using the CAD-ASTRA toolbox [11]. This software package can simulate X-ray projection data based on meshes and allows complete freedom of setup parameters. Here, a source-sample mask distance of $120\,\mathrm{cm}$ and a source-detector distance of $180\,\mathrm{cm}$ were used, creating a geometric magnification of $M = 1.5$. A detector panel with 750 pixels was used.

A. Optical axis shift and IC sampling

In order to perform a first validation of the setup, the shape of the intensity modulation across the detector and the shape of the individual ICs was inspected using simulated flatfield projections. To this end, three different optical axis shifts were tested that respectively span one, three and five ICs across the detector. The corresponding optical axis shift can be calculated using equation 3 with $N = 1, 2, 3$.

Using these simulated flatfields, equation 6 can also be validated by comparing the measured number of IC points to the predicted number of IC points. This is done for a dataset with 75 projection angles and a dataset with 150 projection angles.

B. Inline EI XCT scan

For the full 3D acquisition scan, a mesh of an avocado containing internal defects was used. This mesh was created using real data gathered from an attenuation-based X-ray CT scan using our FleXCT scanner [14]. The resulting mesh is scaled to fit inside the FOV. The attenuation coefficient and refractive index of this mesh can be freely selected. For the avocado shell, we assigned values of $\mu = 0.358\,cm^{-1}$ and $\delta = 1 \times 10^{-7}$. The defects were modeled using the same attenuation coefficient, but with a higher refractive index decrement $\delta = 2 \times 10^{-7}$. The pit was represented with $\mu = 0.404\,cm^{-1}$ and $\delta = 3 \times 10^{-7}$. These values create a scan that shows clear phase signal while the attenuation signal is diminished. This aligns with reality, where different soft tissues have near identical attenuation coefficients, but the refractive indexes differ more. The optical axis shift performed on the mask neatly spans one IC across the detector, resulting in 1499 total projections. These are divided over 95 angles starting from $0°$ and going up to $360°$. If we use equation 6, this leaves us with 8 sample points for almost all ICs. Both attenuation and phase reconstructions are made from a central slice using filtered back projection (FBP).

IV. Results and Discussion

A. Optical axis shift and IC sampling

In Fig. 5, The intensity modulations created on the detector are shown for the values $N = 1, 2, 3$. Respectively one, three and five ICs are neatly spanned across the detector as expected. We found that adding a small compensation term to the denominator of equation 2 (e.g. $1/6b$) helped with the

fitting process of the ICs. If no term was added, the tails of the ICs were not sufficiently sampled. This resulted in bad parameter estimations, as the fitted Gaussian curves appear to have a slight offset. This occurs because equation 3 is based on a point source, while a source with a finite spot size was used in the simulations. N controls the number of peaks by increasing or decreasing the needed optical shift. The shifts are rather small here. This is a result of the large detector size of 750 columns. It can also be noted that the different ICs on the detector have relatively large gaps in between them. This can be explained by the width of the beamlets, which is a lot smaller than the detector mask bar width. The beamlets thus require a big shift before entering the adjacent detector aperture.

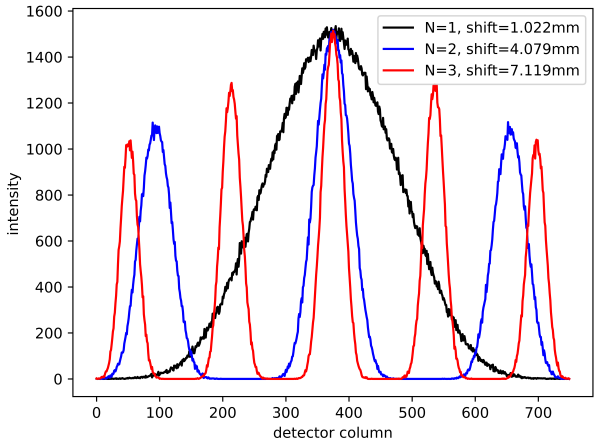

Fig. 5: The illumination modulation created across the detector for three different values of N. The noise on these curves is a consequence of the implementation strategy of finite sources in the CAD-ASTRA toolbox.

Fig. 6 shows two random ICs, one for a flatfield dataset with 75 projection angles and one for a dataset with 150 projection angles. When 75 angles are scanned, 10 IC points are sampled. For 150 angles, only 5 IC points are sampled. This corresponds with equation 6: $N_{IC} = N_{columns}/N_{angles}$. Both curves show another difference: for the IC with 75 angles, the right tail is sampled more than the left. For the IC with 150 angles, the left tail is sampled better. This a consequence of the movement scheme, where rotations and translations are mixed. Before two successive IC points are measured, the sample needs to make a full rotation. Some ICs will be sampled at the beginning of the first full rotation, while others are sampled at the end. This determines the position of the first and last IC point and consequently which tail is sampled better. To avoid an undersampling of these tails, it is important that enough IC points are chosen during acquisition. Alternatively, the optical axis shift can be increased to capture more of the tail by increasing the compensation term. This becomes more important if N is increased, where the coverage of the tails at both ends of the detector diminishes (see Fig. 5).

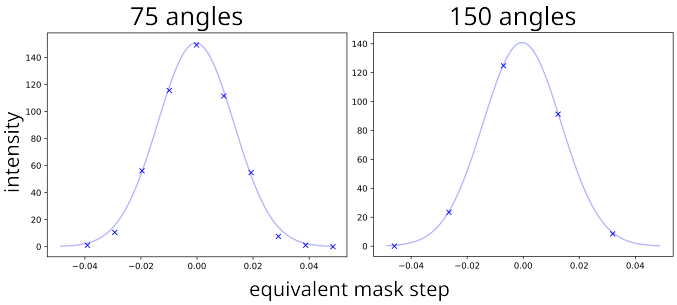

Fig. 6: The IC curves of two different pixels for a different angular coverage illustrated with an opaque blue line. The sampled IC points are shown using a blue cross.

B. Inline EI XCT scan

The attenuation and phase reconstructions can be seen in Fig. 7a. The pit and shell of the avocado are clearly visible in both reconstructions. However, the defects are more clearly visible in the phase reconstruction (e.g. at the bottom of the sample). These defects are also visible in standard out-of-focus EI radiography, but this is not always the case (depending on the projection angle and internal structure). The main advantage of EI XCT is that these defects can also be localized in space. More information is gained about the sample and its defects, which can be invaluable information in industrial settings. Both reconstructions contain streaking artifacts. This is a consequence of the low number of scanned angles and the use of FBP for the reconstructions. Alternatively, iterative techniques with constraints such as total variation minimization can be used. Another option is to increase the detector size. This increases the total number of projections, allowing more angles to be covered (see equation 6).

In Fig. 7b, a reconstruction of the same sample is shown, using the conventional EI setup. Similar to the out-of-focus EI XCT simulation, 95 angles were used with 8 IC points. The out-of-focus approach and the conventional approach clearly give very similar results, but subtle differences in contrast can be noticed. This could be a cone beam effect. In conventional EI XCT, every IC is fully sampled by one beamlet using sample mask steps. For out-of-focus EI XCT, IC sampling is done by multiple beamlets. Every beamlet makes a different angle with the optical axis, which could have a small impact on the fitting process of the ICs (e.g. due to shadowing of the detector mask). The biggest difference between both methods is the number of projections. The conventional method takes 750 projections while the out-of-focus methods requires almost double that. However, in inline settings where multiple samples are scanned in rapid succession, the mean number of projections can be reduced back to 750 by aligning their FOVs.

The conventional EI technique allows the retrieval of an additional contrast: dark-field. While the proposed out-of-focus EI-XCT method can, in theory, also retrieve this information, the evaluation of dark-field contrast was not a subject of this study and is left for future work.

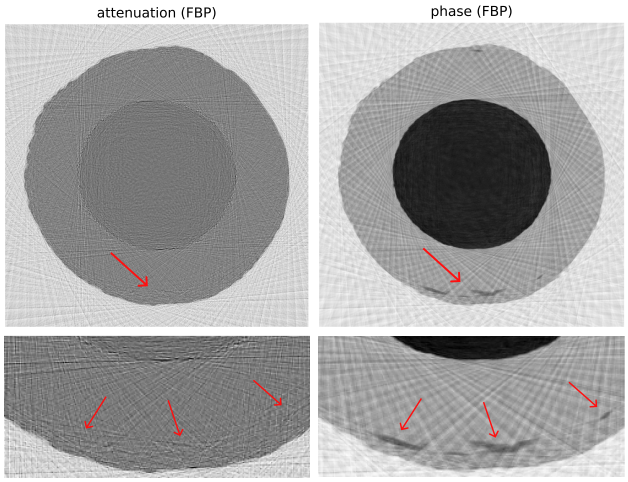

(a) Reconstructions using the out-of-focus EI XCT setup.

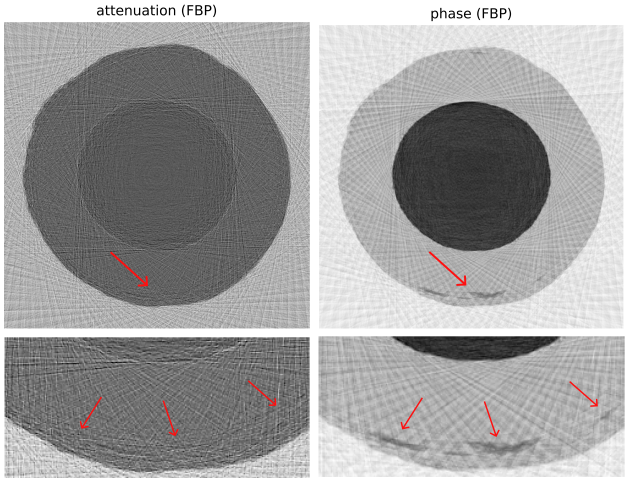

(b) Reconstructions using the conventional EI XCT setup.

Fig. 7: Attenuation and phase reconstructions of the avocado mesh using both the out-of-focus approach and a conventional EI approach. Zoom-ins on some defects in the avocado are shown on the bottom rows. FBP was used for the reconstructions.

V. Conclusion

In this paper, an inline phase contrast XCT method based on the out-of-focus EI technique [10] is presented. The number of projection angles and number of IC points can be easily adapted by changing the angle between two successive projections and the optical axis shift. No new hardware is required in comparison to a conventional EI XCT setup. Using the proposed method, more sample information can be gained than using radiography-based inspection techniques. For example, in inline industrial settings, out-of-focus EI XCT can be used to better visualize and localize certain structures and defects. However, as no setup modifications are made in comparison with out-of-focus EI X-ray radiography, a switch between the two can easily be made. This allows for an acquisition scheme that provides both high throughput and high IC sampling using out-of-focus EI X-ray radiography and optimal structure localization using out-of-focus EI XCT, purely by adding rotation.

References

[1] A. Karme, A. Kallonen, V.-P. Matilainen, H. Piili, and A. Salminen, "Possibilities of ct scanning as analysis method in laser additive manufacturing," *Physics Procedia*, vol. 78, pp. 347–356, 2015.

[2] A. Guelpa, A. du Plessis, and M. Manley, "A high-throughput x-ray micro-computed tomography (μ ct) approach for measuring single kernel maize (zea mays l.) volumes and densities," *Journal of Cereal Science*, vol. 69, pp. 321–328, 2016.

[3] Q. Zhao, Z. Gao, H. Wang, H. Wu, X. Chen, Z. Qu, T. Zhao, and D. Fang, "On accurate characterization of interfacial morphology and damage evolution of thermoplastic composite welded joints: A microscale study via in-situ micro-ct," *Composites Science and Technology*, vol. 236, p. 110004, 2023.

[4] S. C. Garcea, Y. Wang, and P. Withers, "X-ray computed tomography of polymer composites," *Composites Science and Technology*, vol. 156, Oct. 2017.

[5] S.-X. Wang, R. Hu, K. Gao, F. Wali, B. Zan, D.-J. Wang, Z.-Y. Pan, and S.-Q. Wei, "Non-destructive study of fruits using grating-based x-ray imaging," *Nuclear Science and Techniques*, vol. 28, Feb. 2017.

[6] A. F. T. Leong, E. Asare, R. Rex, X. H. Xiao, K. T. Ramesh, and T. C. Hufnagel, "Determination of size distributions of non-spherical pores or particles from single x-ray phase contrast images," *Opt. Express*, vol. 12, pp. 17 322–17 347, Jun. 2019.

[7] A. Olivo, "Edge-illumination x-ray phase-contrast imaging," *Journal of Physics: Condensed Matter*, vol. 33, p. 363002, Jul. 2021.

[8] P. C. Diemoz, C. K. Hagen, M. Endrizzi, M. Minuti, R. Bellazzini, L. Urbani, P. De Coppi, and A. Olivo, "Single-shot x-ray phase-contrast computed tomography with nonmicrofocal laboratory sources," *Phys. Rev. Appl.*, vol. 7, p. 044029, Apr. 2017.

[9] M. Endrizzi, A. Astolfo, F. Vittoria, T. Millard, and A. Olivo, "Asymmetric masks for laboratory-based x-ray phase-contrast imaging with edge illumination," *Scientific Reports*, vol. 6, p. 25466, May 2016.

[10] N. Francken, J. Sanctorum, J. Sanctorum, P.-J. Vanthienen, J. Sijbers, and J. De Beenhouwer, "Inline edge illumination x-ray phase contrast imaging through mask misalignment," *Optics Express*, vol. 32, pp. 32 048–32 061, Aug. 2024.

[11] P. Paramonov, N. Francken, J. Renders, D. Iuso, T. Elberfeld, J. D. Beenhouwer, and J. Sijbers, "Cad-astra: A versatile and efficient mesh projector for x-ray tomography with the astra-toolbox," *Optics Express*, vol. 32, pp. 3425–3439, 2024.

[12] A. V. Bronnikov, "Theory of quantitative phase-contrast computed tomography," *J. Opt. Soc. Am. A*, vol. 19, pp. 472–480, Mar. 2002.

[13] C. K. Hagen, F. A. Vittoria, O. R. i. Morgó, M. Endrizzi, and A. Olivo, "Cycloidal computed tomography," *Phys. Rev. Appl.*, vol. 14, p. 014069, Jul. 2020.

[14] B. D. Samber, J. Renders, T. Elberfeld, Y. Maris, J. Sanctorum, N. Six, Z. Liang, J. D. Beenhouwer, and J. Sijbers, "Flexct: a flexible x-ray ct scanner with 10 degrees of freedom," *Optics Express*, vol. 29, pp. 3438–3457, Feb. 2021.